

Numerical simulation and experimental analysis of solid state sintering response of 316L stainless steel micro-parts manufactured by metal injection molding

M. Sahli^{1,2}, A. Lebled², J-C. Gelin¹, T. Barrière¹ and B. Necib²

¹FEMTO-ST Institute / Applied Mechanics Department, ENSMM, 24 chemin de l'épitaphe, 25000 Besançon, France

²Laboratory of Mechanics, Faculty of Engineering Sciences, Mentouri-Constantine University, Road of Ain-el-Bey, 25000, Constantine, Algeria
Mohamed.sahli@ens2m.fr

Abstract. The metal injection molding process allows the manufacturing of small and very complex metallic components. Metal injection molding processing combines the shaping capability of polymer injection moulding with the large material variety of metals. This paper discusses in detail the development of a numerical model capable of simulating structural evolution and macroscopic deformation during sintering of complex micro-gears compacts. A sintering model based on elastic-viscoplastic constitutive equations was proposed and the corresponding parameters such as sintering stress, bulk and shearing viscosities and were identified from dilatometer experimental data. The constitutive model was then implemented into finite element software in order to perform the simulation of the sintering process. The numerical predictions of shrinkages and densities were compared with experimental measurements, and it is shown that the results numerically simulated by finite element agree well with those experimentally observed. The experimental data were obtained from sintering of stainless steel powders.

Keywords: Sintering, shrinkage, modeling simulation, feedstock, metal injection molding

1. Introduction

The Metal Injection Moulding (MIM) is a manufacturing technology that combines the shaping efficiency of plastic injection moulding with the capability of powder metallurgy for processing metal powders. It permits to get net shape components with complex geometry from polymers combined with metals [1-3]. This process is used in several fields as automotive and aeronautics, data processing, electronics etc [4, 5]. In this process, a custom formulated mixture of an extremely fine metal powder and wax-polymer based binders are initially blended into a mouldable formulation. The binder transports the metal powder to fill out the desired geometry. The green component, which consists of two materials with a low cohesive force, cannot be used in this form for most applications because material properties such as strength and modulus are very low, thus it must be debound and sintered. In thermal debinding, the binder diffuses through the pores to the component external surfaces where it is removed as vapour. At the end of the thermal debinding the

component is considered brown and ready for sintering [6]. During sintering, the separate particles are welded together and develop the final mechanical properties (See Fig. 1).

The modelling of the MIM process requires being able to know the final shape after injection and also the spatial powder volume fraction in order to be able to compute the final density. From the technological point of view, the dimension control is one of the most important practical problems in sintering where the final product configuration is conditioned by spontaneous densification. Dimensional control is therefore a critical issue in sintering technology because post-processing is expensive and can introduce damage. In this connection, the modelling of the macroscopic behaviour of the components under sintering is necessary.

There have been several attempts to model, and explain theoretically, compaction and sintering of powder [8-10]. A continuum mechanics model for explaining densification and deformation behaviour of a porous material [11-13] relies on an extended yield function that includes a hydrostatic pressure term. Various models for describing sintering behaviour have also been proposed [14-16]. The basic sintering model consisted of a two dimensional model with a single diffusion mechanism but was later expanded to describe multiple transport mechanisms, sintering stages, and pressure-assistant sintering [8, 17]. Tselikh et al. [18] suggested an empirical finite element analysis. Schoenberg et al. [19] compared analytical calculations and FE simulations to describe the sintering of a barium titanate cylindrical component composed of a high-density and low-density layer. Song et al. [20] investigated simulating the sintering process of 316L stainless steel powder components with a thermo-elasto-viscoplastic model. Kuczynski [21] studied mechanisms for neck growth and shrinkage during early sintering stages (particle bonding) using a two-sphere model. Coble [22] developed a cylindrical pore model. A spherical pore model for the later sintering stages was developed by MacKenzie and Shuttleworth [23]. Barriere et al. [24, 25] investigated the optimal process parameters by proposing adapted finite element modelling and simulation software for the Metal Injection Moulding stage (MIM) based on a bi-phasic model. Nosewicz et al. [26] presents an original viscoelastic model of powder sintering developed within the discrete element framework. This model has been applied to the simulation of real process of sintering of NiAl powder. The model reproduces correctly the mechanism of free sintering and sintering under pressure. Mohsin et al. [27] suggested a finite element analysis based on a thermo-kinetic model to describe the densification process of a MIM copper brown body during sintering.

This paper focus on the measuring thermo-physical properties and numerical simulation associated with the sintering process. It was also reported that the force of gravity and inhomogeneity of the particle distribution can be made the comparison difficult between experimental results and The FE model data. Furthermore, some enhancements are suggested in temperature field calculation of FE model in order to draw a real furnace conditions. Heaney et al., [28] investigated the reliability of numerical simulations for the prediction of the shrinkage of a metal injected moulded component. The main results obtained have been the possibility to simulate the entire process of binder removal and component densification by evaluating the entire stress/stain history. The FE model has allowed the evaluation of main displacements of the component during all process steps, obtaining a good agreement with experimental tests. Jeong et al., [29] developed a unified model for describing compaction and sintering based on plasticity theory. In this paper, a method for predicting the final dimensions of a powder product was proposed. The proposed model simulates the powder process continuously and simultaneously and is more effective than previous models that treat compaction and sintering separately. It was shown that the unified model increases the dimensional accuracy of the final product in the actual powder process.

The objective of the present work was the shrinkages and densities prediction of a MIM micro-component with finite element (FE) method. Thermo-mechanical analyses were performed with a general purpose FE solver (ABAQUS[®]) in order to mimic phenomena acting during sintering stage.

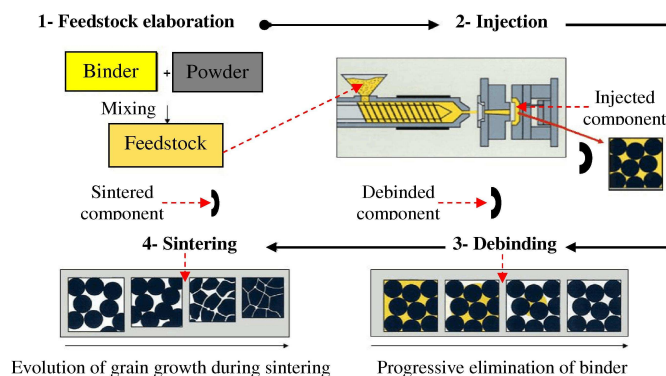


Fig. 1. Schematic diagram of whole PIM process, showing the basic steps from feedstock elaboration stage to sintered component [7].

2. Experimental procedures and result analysis

Fine powders of 316L stainless steel were used to develop the mixtures dedicated to the micro-PIM. The powder particulates had a spherical shape and an average particle size of $5\mu\text{m}$ -80%. This shape is generally more appropriate for obtaining a feedstock with low viscosity. The powders had a density equal to $7.9\text{g}/\text{cm}^3$ and were provided by Sandvik Osprey Company. Figure 2 gives a photograph of the 316L stainless steel powder particle distribution. The binder components were polypropylene (PP), paraffin wax (PW) and stearic acid (SA). The PP primary binder is used to retain the component shape after injection molding and debinding. The main effect of the PW secondary binder is to decrease the feedstock viscosity and increase the replication ability of the feedstock. The SA surfactant is used to facilitate powder wetting. The composition of the binder corresponded to the ratio of PP:PW:SA given as relative fractions 40:55:5. The characteristics of the different binder systems and the raw powders are related in Table 1 and Table 2.

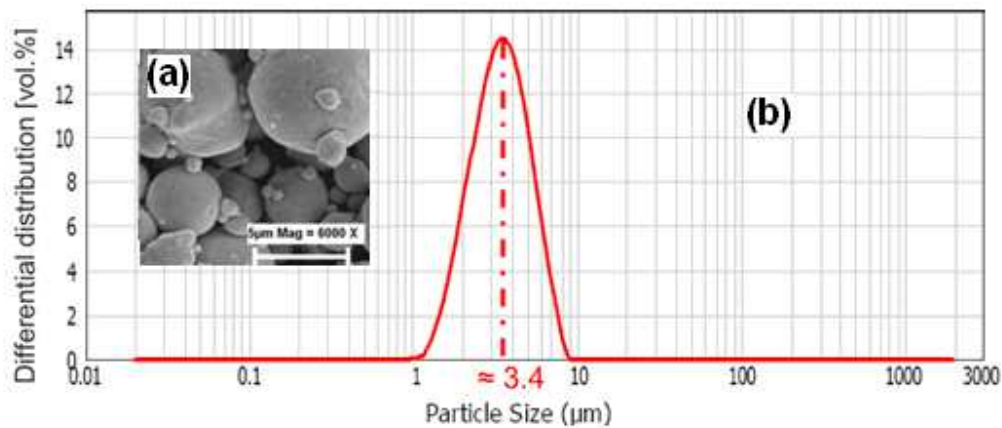


Fig. 2. (a) Scanning electron micrograph of the stainless steel powders, (b) Particle size distribution for the 316L stainless steel powder ($D_{50}=3.4\ \mu\text{m}$) used in this work.

By employing the proposed binder system, 316L stainless steel feedstocks with 60-66% solid loading fraction were used for the experiments. The mixing of the powders and binders was carried out using a twin-screw mixer at 180°C and 30 rpm for 30 min. The powders were loaded when the temperature had stabilised at the required mixing temperature to facilitate homogeneous mixing of the powder and binder components. Fig. 3a illustrates the mixing behaviour of stainless steel

feedstocks with solid loadings of 60, 62, 64 and 66%. Varying the solid loading caused variation in the torque level, indicating differences in the mixture viscosity values. The observed torque peaks are due to the introduction of small amounts of feedstock into the mixture. It should be noted that the mixture with a solid loading of 60% had the lowest torque homogenisation, reaching a value of approximately 0.215 N.m. Therefore, the optimal load of 316L stainless steel powder was identified to be 64%. Beyond a load of 64%, the feedstock did not demonstrate mixability. Fig. 3b shows Scanning Electron Microscope images (SEM) of the feedstock powders after the mixing stage.

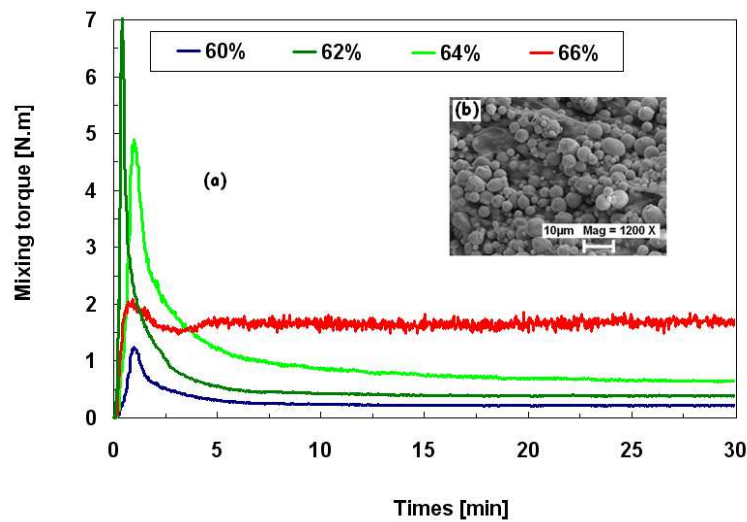


Fig. 3. (a) Mixing torque vs. time for 316L stainless steel feedstocks with different solid loadings, obtained from the mixing test (180 °C, 30 min and 30 rpm), (b) SEM micrographs of the feedstock after mixing, including 316L stainless steel (the solid loading equal to 60%).

Table 1. Characteristics of the different binder components.

Binders	Density [g/cm ³]	Melting temperature [°C]
Stearic acid (SA)	0.89	70
Paraffin wax (PW)	0.91	60
Polypropylene (PP)	0.90	160

Table 2. Characteristics of the stainless steel powders.

Powder	Particle shape	Powder size and density			Density (g/cm ³)	Tap density (g/cm ³)
		d ₁₀ (µm)	d ₅₀ (µm)	d ₉₀ (µm)		
Stainless steel	Spherical	1.80	3.40	6.0	7.90	4.60

The granulated feedstock was injection moulded into mould insert by using a Billon 60H horizontal injection moulding press. A set of suitable injection moulding parameters used is shown

in Table 3. The moulded micro-gears were thermally debound in a furnace according to a suitable debinding profile indicating temperature, time and heating rate. The debinding profile was based on earlier work for the 316L stainless steel feedstock [30]. The highest debinding temperature was set to 600°C to ensure that all the binder components are removed and to facilitate handling. After debinding, the samples were maintained at this temperature for 1 h, and then the temperature was increased between 1000 - 1360°C a rate of 5°C/min, 10°C/min or 15°C/min for 316L stainless steel. Additionally, the same primary vacuum was used during the sintering test.

Table 3. Suitable injection moulding parameters for the micro-part.

Moulding parameters	Value
Injection pressure (MPa)	80
Injection speed (PW)	0.91
Melting temperature (°C)	180/180/190/200
Mould temperature (°C)	25

During thermal debinding and sintering, binder elimination and subsequent particles bonding take place, resulting in dimensional change of the PIM parts. The linear shrinkage of many MIM parts is in the range of 14% to 18%. Fig. 4 shows the photograph of the micro-gears after undergoing different processing steps. Compared with the moulded part, the dimensional change after debinding was not noticeable whilst the dimensional change after sintering was clearly evident. This was in agreement with the outer diameter change for the micro-gears as shown in Fig. 5. It can be seen that the apparent decrease in the diameter of the micro-gears occurred after sintering.

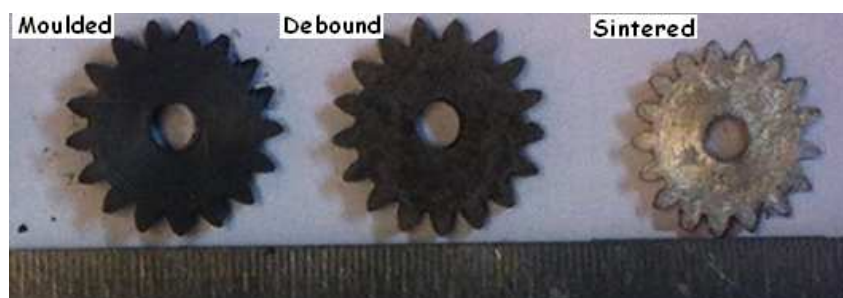


Fig. 4. Photograph of the micro-gears after different processing steps

Fig. 5 shows the average dimensions of the micro-gears after undergoing different processing steps. The dimensional changes in diameters and thickness of the micro-parts showed similar trend. Compared with the die cavities mould insert, the diameters and thickness of the molded micro-gears

increased slightly. This was because the volumetric expansion due to cavity pressure decrement prevailed the volumetric shrinkage from cooling. However, the diameters and thickness of the micro-gears tended to decrease slightly after debinding. The diameters and thickness of the micro-gears decreased gradually from sintering temperature of 1050°C to 1150°C. Above 1150°C, the diameters and thickness of the micro-gears were relatively close and were smaller than that of the mould insert. As example, the shrinkage of the root diameter of the gears was 13.85% at 1150°C. In the temperature range between 1200°C and 1360°C, the shrinkages of the diameters were close, around $\approx 14\%$. The shrinkages of the micro-gears increased with sintering temperatures below 1360°C. At 1360°C and above, the shrinkages were independent of the sintering temperatures (see Fig. 5).

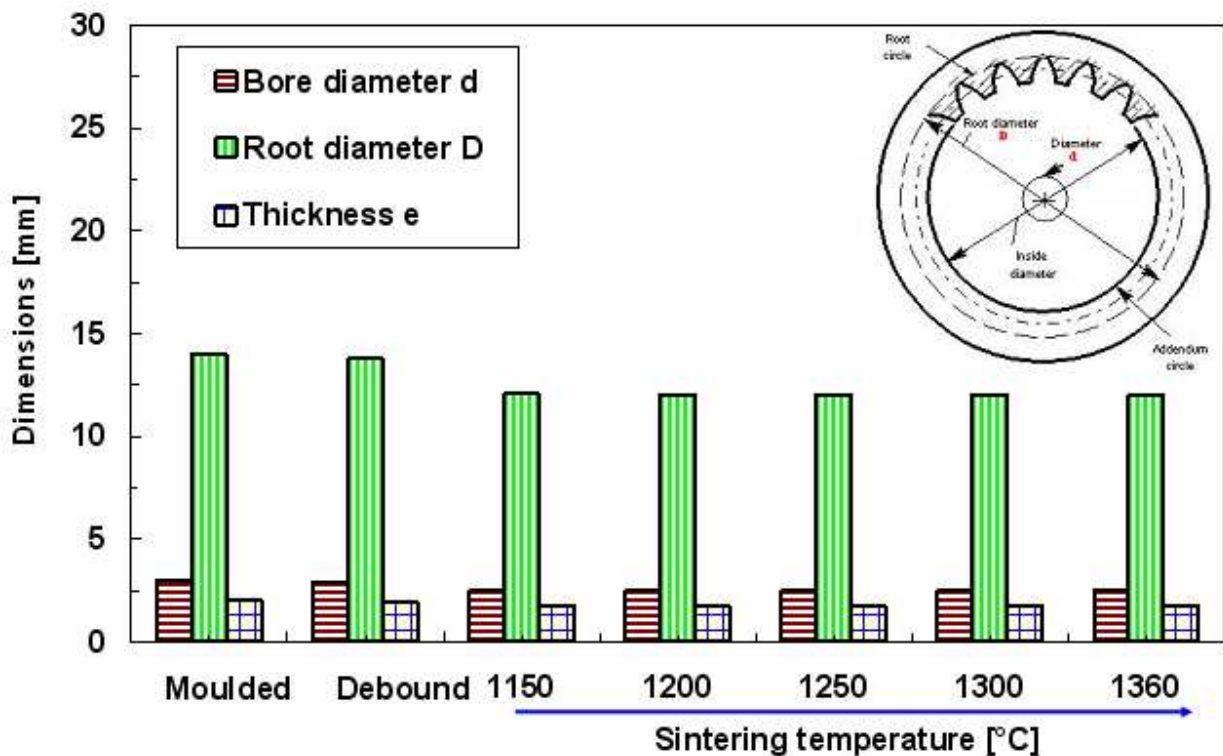


Fig. 5. Dimensions of micro-gears after different processing steps (solid loading: 62%, sintering rate: 5°C/min).

Additionally, the densities of the sintered micro-gears were measured with the water displacement method (the Archimedes method) for each of the three feedstocks, and the resulting values are reported in Fig. 6. Fig. 6 shows the densities of the sintered micro-gears at different temperatures. The sintering temperature and solid loading both had a significant effect on the

densification, i.e., the density increased significantly with increasing temperature and solid loading, as summarised in Fig. 6. No significant density change was observed for sintering temperatures of 1360 °C and above, which was in agreement with the result of the dimensional change. The relative densities of the sintered micro-gears were determined to be above 90% of the theoretical density of the material.

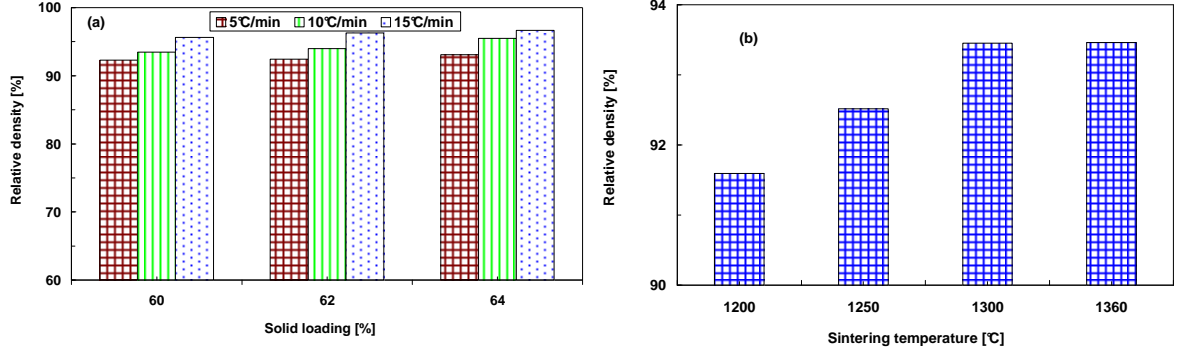


Fig. 6. Relative densities of the micro-gears sintered: (a) at 1360°C with different solid loading and (b) sintering temperatures (solid loading 60%).

3. Numerical simulation of the sintering process

3.1. Modeling of the sintering process

To simulate the sintering process using a finite element method, several macroscopic models have been developed to predict the shrinkages and distortions of the components during the sintering process. In these works, the sintering body is regarded globally as a compressible continuum even though it is composed of a solid and pores. Green components are usually elastic at room temperature, and an elastic to viscous transition during sintering. The viscoplastic constitutive law in continuum mechanics can be used to describe this transition. The total strain ε of this model is:

$$\dot{\varepsilon} = \dot{\varepsilon}_e + \dot{\varepsilon}_{th} + \dot{\varepsilon}_{vp} \quad (1)$$

where $\dot{\varepsilon}$ is the total strain rate, $\dot{\varepsilon}_e$ is the elastic strain rate, $\dot{\varepsilon}_{th}$ is the thermal strain rate and $\dot{\varepsilon}_{vp}$ is the viscoplastic strain rate. The elastic strain and thermal strain are due to the change in the sintering temperature.

The elastic strain rate is assumed to be linear and isotropic and can be expressed with the following Hooke's law:

$$\dot{\epsilon}_e = C_e \dot{\sigma} \quad (2)$$

The thermal strain rate $\dot{\epsilon}_{th}$ is mainly due to thermal expansion, which can be expressed as:

$$\dot{\epsilon}_{th} = \alpha \Delta \dot{T} I$$

At a high sintering temperature, viscoplastic strain is more dominant and overcomes the elastic strain. The viscoplastic strain rate is given by the following equation:

$$\dot{\epsilon}_{vp} = \frac{dev(\sigma)}{2G} + \frac{\sigma_m - \sigma_s}{3K} I$$

where C_e is the elastic compliance matrix, α is the thermal expansion coefficient, $\Delta \dot{T}$ is the incremental temperature rate, I is the second order identify tensor, α is experimentally determined using a dilatometer, $\sigma_m = tr(\sigma)/3$ is the trace of the stress tensor, G is the shear viscosity modulus, K is the bulk viscosity modulus, and σ_s is the sintering stress. The variables G , K and σ_s are material parameters that still need to be determined.

The elastic-viscous analogy is used to define the shear and bulk viscosity moduli for sintering materials [31]:

$$G_p = \frac{\eta_p}{2(1+\nu_p)}, K_p = \frac{\eta_p}{3(1-2\nu_p)} \quad (2)$$

where η_p and ν_p are the uniaxial viscosity and the viscous Poisson's ratio of a porous material, respectively. Song et al. [32] derived the following relationship to define the uniaxial viscosity η_p^e through bending tests in a dilatometer:

$$\eta_p^e = \frac{1}{\delta} \left(\frac{5\rho_a g L_s^4}{32h^2} + \frac{PL_s^3}{4bh^3} \right) \quad (3)$$

where $\dot{\delta}$ is the deflection rate at the centre of the specimen, ρ_a is the apparent density, g is gravity, P is the external load, and L_s , b and h are the distance between the two supporting rods and the width and thickness of the specimen, respectively. The viscous Poisson's ratio is determined from [32]:

$$v_p \approx \sqrt{\frac{\rho}{3-2\rho}}, \quad \rho = \frac{\rho_0}{(1+\lambda)^3} \quad (4)$$

where ρ is the relative density ρ_0 and λ is the uniaxial shrinkage, which is defined as:

$$\lambda = \frac{L-L_0}{L_0} \quad (5)$$

where L_0 and L are the length of the specimens before and after sintering.

The following equation is used to determine the sintering stress [33]:

$$\sigma_s = B\rho^C \quad (6)$$

where B and C are material parameters identified from dilatometry experiments. Using these proposed constitutive equations, the related material parameters can be determined.

3.2. Sintering parameter identification

The identification algorithm is designed for the proper identification of material parameters B and C used in the sintering stress model to optimise the numerical simulations (see Table 4). The following equation was proposed to calculate the stress during the sintering stage [33]:

$$\frac{1}{L} \frac{dL}{dt} = \alpha \Delta \dot{T} - \frac{1}{3K_p} \sigma_s \quad (7)$$

The proper strategy consists of identifying parameters B and C in Matlab[®] that determine the numerical shrinkage curve according to equation (8). This curve is matched to that obtained from the free sintering tests. Therefore, the minimisation algorithm is used to fit the simulations as best as possible to the experimental curves by adjusting the physical parameters [14]:

$$\begin{cases} \min F(x) \\ F(x) = \sum_{i=1}^n |\lambda^m(T_i, x) - \lambda^e(T_i, x)|^2 \\ x = [B, C] \end{cases} \quad (8)$$

where λ^e is the experimental uniaxial shrinkage obtained from the dilatometry tests, λ^m is the numerical uniaxial shrinkage, $F(x)$ is the mean residual squares of the tolerance, where $i=1, \dots, n$ indicates the different sintering temperatures and x is the set of material parameters that need to be identified.

Material parameters were determined by the beam-bending tests for the 316L stainless steel feedstock at high solid loadings from 60% to 66% using the vertical dilatometer. The sintering temperatures of the 316L stainless steel powders are from 1050°C to 1360°C. In addition, heating rates of 5°C/min, 10°C/min and 15°C/min were used for identification tests. The setup used for the beam-bending tests in a SETSYS[®] vertical dilatometer is shown in Fig. 7. The associated probe is made up of a base with two knives and a rod with a knife-shaped cross section. A load equal to 5 cN was applied at the centre of the specimen through the rod. The specimens have a rectangular shape of 14 mm in length; 5.5 mm in width and 1 mm in thickness (see Fig. 7b).

The uni-axial viscosity curve vs. the different sintering temperatures for the different loaded 316L stainless steel feedstocks were observed and shown in Fig. 8. For identical heating rates, the higher the feedstock solid loading, the higher the uniaxial viscosities are at the same temperature. This is related to the fact that the more powder used, the higher the related viscosity becomes.

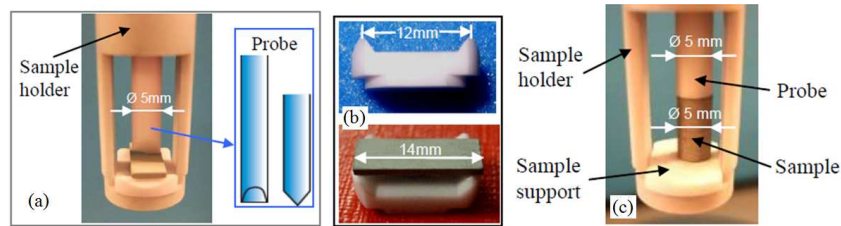


Fig 7. Beam-bending test in a vertical SETSYS[®] evolution dilatometer: (a) Setup for the TMA measurement and the probe, (b) geometry of the sample and the sample support and (c) setup for free-sintering test.

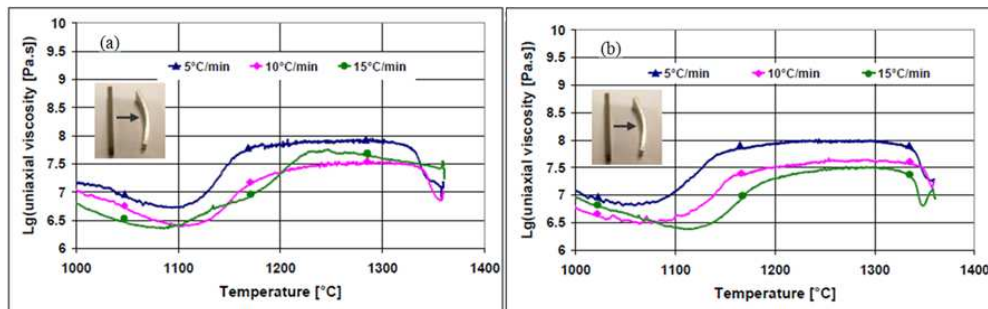


Fig 8. Uni-axial viscosity vs. temperature from the beam-bending tests conducted in a vertical dilatometer for 316L stainless steel feedstock at solid loadings of (a) 62% and (b) 64%.

Complementary tests were performed in a compression configuration using a vertical dilatometer, as indicated in Fig. 7c. The length of the cylindrical specimens is 10 mm, and the diameter is 5 mm. The rod and base both have flat surfaces. The uniaxial shrinkage curve vs. the different sintering temperatures for the 316L stainless steel feedstocks were observed and shown in Fig. 9. Shrinkage begins to occur at approximately 1000°C and rapidly increases at a temperature above 1050°C until approximately 1200°C. At the same temperature, significant shrinkage is obtained for the specimens fabricated at lower powder loading. The reason is that when the powder loading is high, more pores are produced and the components shrink more obviously after sintering.

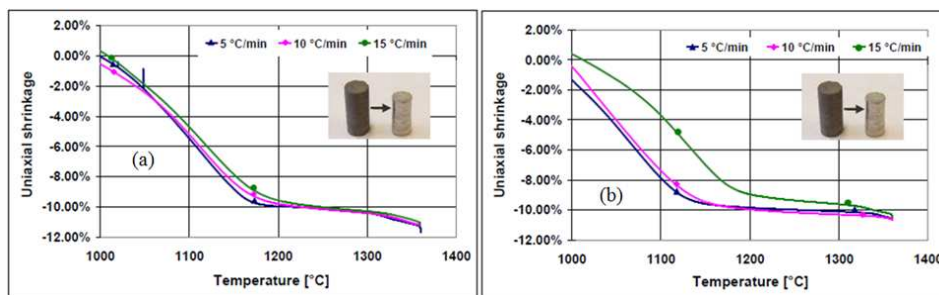


Fig 9. Uni-axial shrinkage vs. temperature from free-sintering tests in a vertical dilatometer for the 316L stainless steel feedstock at powder volume loadings of (a) 62% and (b) 64%.

Table 4. Material parameters B and C used in the sintering process for the stainless steel feedstock

Stainless steel feedstock		$\rho < 0.8$		$\rho \geq 0.8$	
		B (Pa)	C	B (Pa)	C
60%	5 °C/min	3.91×10^7	0.30	1.47×10^{-1}	-93.13
	10 °C/min	7.26×10^8	9.79	5.73×10^2	-58.77
	15 °C/min	1.13×10^8	3.74	3.04×10^4	-39.42
62%	5 °C/min	6.50×10^3	5.25	2.48×10^3	-5.43
	10 °C/min	$1.11 \cdot 10^3$	0.05	1.53×10^3	-6.33
	15 °C/min	6.76×10^3	4.65	1.70×10^3	-8.79
64%	5 °C/min	7.15×10^3	5.23	8.52×10^2	-10.41
	10 °C/min	3.98×10^3	3.35	3.09×10^3	1.22
	15 °C/min	6.20×10^3	4.64	2.08×10^2	-23.27
66%	5 °C/min	3.09×10^3	3.73	2.44×10^3	-6.17
	10 °C/min	-	-	-	-
	15 °C/min	-	-	-	-

4. Finite element modeling and results analysis

4.1. Boundary and initial conditions

Predicting uneven shrinkage of the sintering part is one of the important purposes of sintering simulation. Several factors such as gravity, inhomogeneous green density, and friction between the supports and the parts should be considered. The following simulations are realized to analyze the influences of these factors. The initial geometry of the FE model was the mesh of the injection moulded component obtained with ABAQUS[®] used for the injection step is related through Fig. 10. The plate support is assumed to be a rigid body during the simulation, and the coefficient of friction between the specimens and the graphite support is set at 0.1. The plate support and the micro-component elements considered for the simulation are R3D4 and C3D8R elements, respectively. In addition, the « Pressure/Over-closure » contact was selected for the components. The material was modelled using the constitutive equations defined in the previous paragraphs, also considering isotropic thermal and mechanical properties.

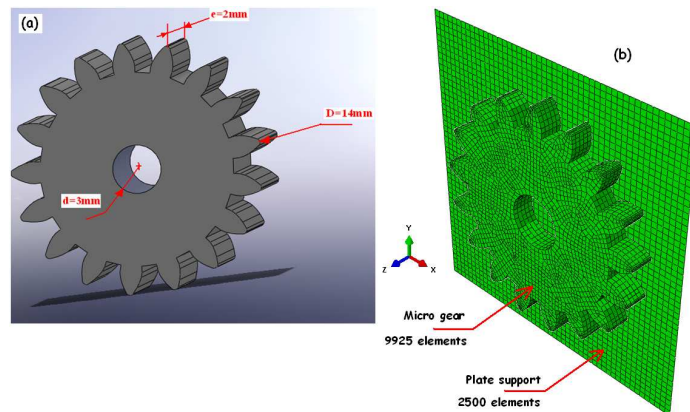


Fig. 10. (a) 3D CAD model of the spur gears and (b) FE meshes of the micro-gears and the plate support prior to the simultaneous sintering stages.

4.2. Numerical results and discussion

Figure 11 shows the predicted numerical shrinkage distribution for the micro-gears after sintering at different temperature of 1050°C, 1150°C, 1250°C and 1360°C, respectively. At 1050°C, there is very few shrinkage of sample. The shrinkage of the sample sintered at 1360°C increases to 14.45% from its original. The maximum shrinkage occurs at the tooth surfaces and illustrates the distortion often induced in the final sintered component. The radial shrinkage in the micro-gears at different sintering temperature is related in Fig. 12. The results of all these simulations show isotropic shrinkage behaviour; this is due to the axisymmetric of the spur gear geometry. The maximum of the isotropic shrinkage have been observed on the teeth of the sprocket, and obtained for a thermal kinetics corresponding to 10°C/min. Total shrinkage rate is shown in Fig. 13 for three different heating rates. It increases with increasing heating rate. It clearly seen that the shrinkage value was stable and homogeneous at 10°C/min.

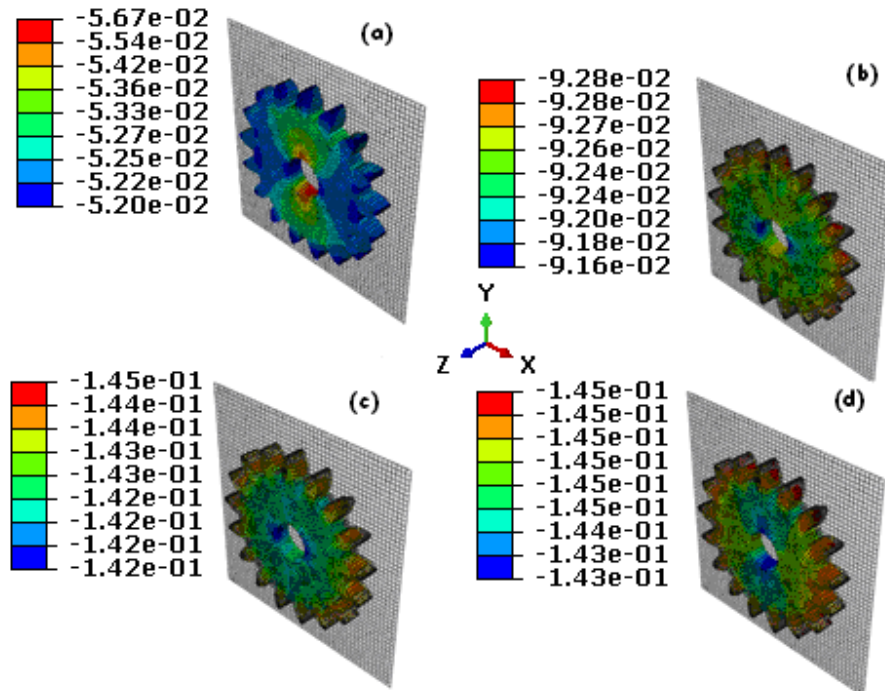


Fig. 11. Numerical final shrinkage of the sintered micro-gears versus sintering temperature: (a) 1050°C, (b) 1150°C, (c) 1250°C and (d) 1360°C (heating rate: 10°C/min, solid loading of 64% - unit %).

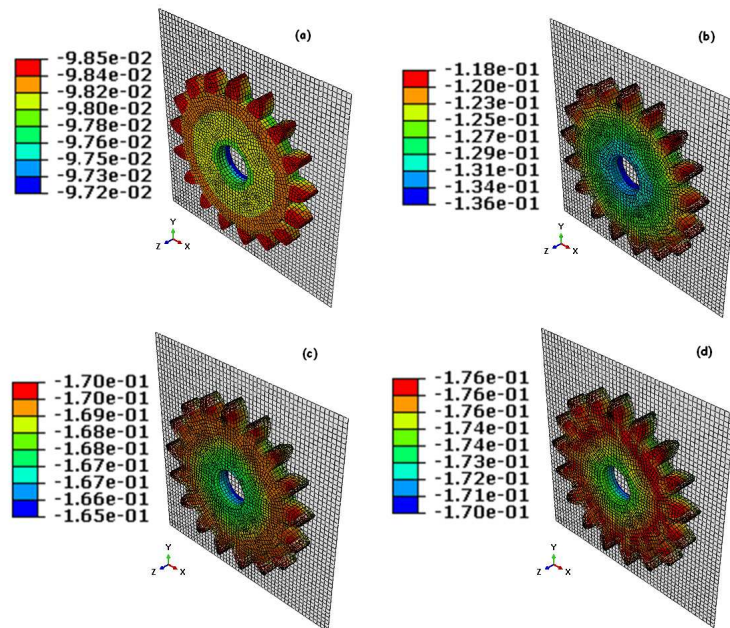


Fig. 12. Numerical radial shrinkage of the sintered micro-gears versus sintering temperature: (a) 1050°C, (b) 1150°C, (c) 1250°C and (d) 1360°C (heating rate: 10°C/min, solid loading of 60% - unit %).

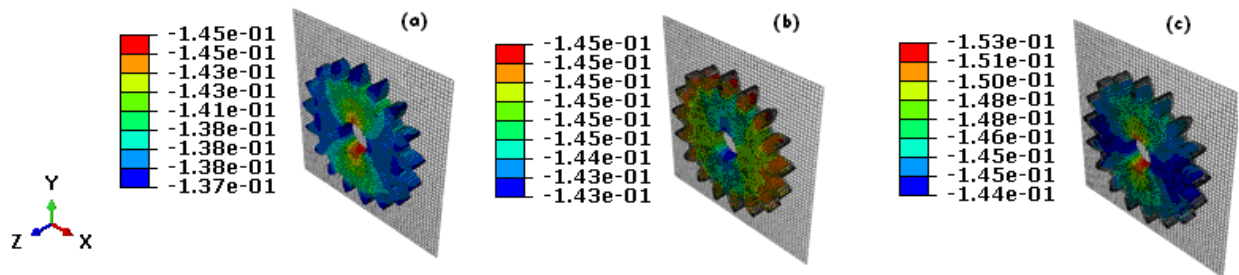


Fig. 13. Numerical final shrinkage of the sintered micro-gears versus heating rate: (a) 5°C/min, (b) 10°C/min and (c) 15°C/min (sintering temperature: 1300°C, solid loading of 64% - unit %).

As shown Figure 14, when solid loading is increased, shrinkage was decreased. The micro-gear loading with 64% solid was optimum for 316L stainless steel feedstock, which showed the best physical properties. This agrees with previous results, which suggest that optimum solid loading of stainless steel was 60%. Figure 15 shows the stress values of 316L sintered at three different temperatures. The sintered micro-gears show the same mechanical behaviour. It can be observed that the final stress distribution is still almost uniform and without warpage. For the small parts like micro-gears, the gravity has little effects on the densification if the support manner is chosen suitably in sintering.

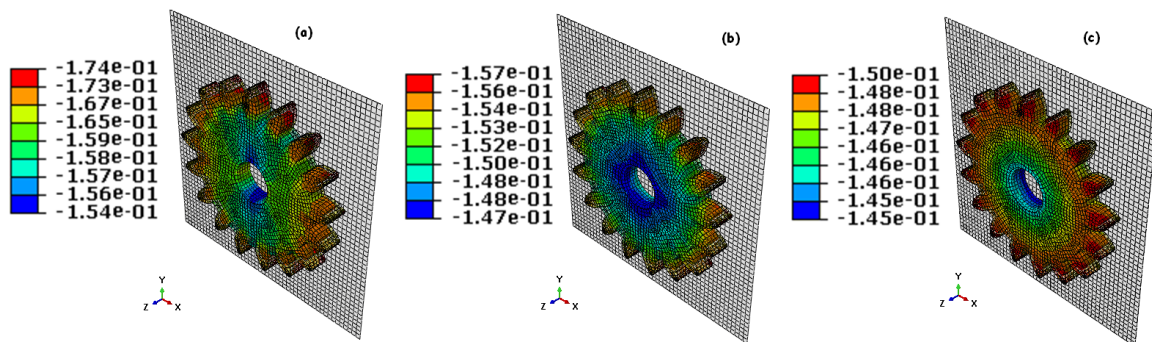


Fig. 14. Numerical final shrinkage of the sintered micro-gears versus solid loading: (a) 60%, (b) 62% and (c) 64% (sintering temperature: 1360°C, heating rate: 10°C/min - unit %).

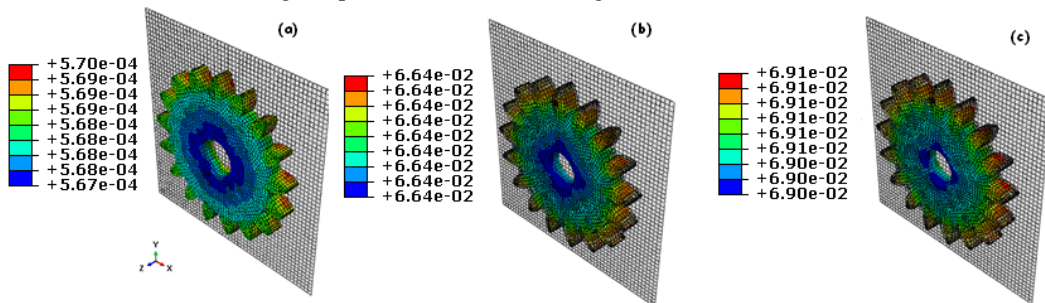


Fig. 15. Numerical final stress of the sintered micro-gears versus sintering temperature: (a) 1150°C, (b) 1250°C and (c) 1360°C (solid loading: 62%, heating rate: 10°C/min), unit: GPa.

The homogeneity of the green parts is induced by the previous processes before the sintering, such as the mixture of powders and binders, pressing or injection moulding [34-36]. In the present study, the simulation is carried out with a green part assumed homogeneous after injection stage. Its relative density varied from 0.6 to 0.64.

Besides of shrinkages, the relative densities have been simulated as well for these micro-gears injected with solid loading of 60%, 62% and 64%, respectively. The relative density distributions of the sintered micro-gears have been illustrated in Fig. 16. As it is shown in the figures, the relative densities are generally homogeneous for most of the simulations, in which the variations have been well controlled within 3%. However, some little better results have been obtained in the first and second ones (solid loading: 60% and 62%, heating rate: 10°C/min). It has been shown also that the components loaded higher are particularly more sensitive to the rapid heating rate. Figure 17 shows the effect of the solid loading on the relative density values of micro-gears after sintering stage at 1360°C. It can be seen that the relative density of micro-gears increases steadily with increasing of solid loading. This indicated that the increase of the solid loading is in favour of the densification of micro-gears.

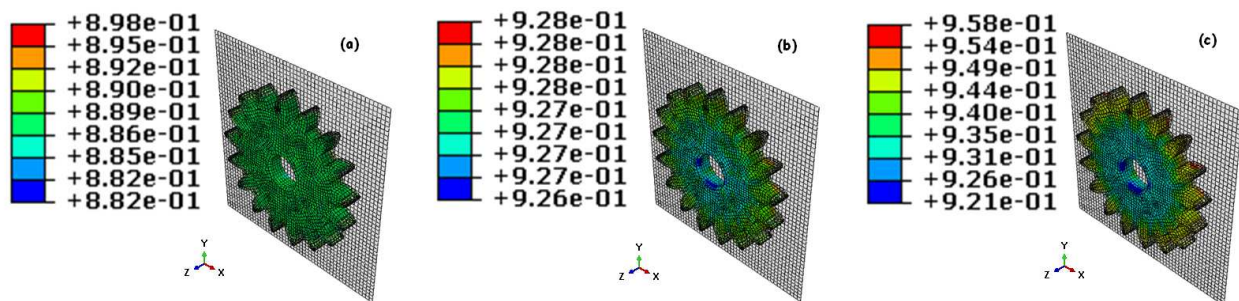


Fig. 16. Final distribution of the relative density in the micro-gears after sintering, obtained numerical simulation: (a) 60%, (b) 62% and (c) 64% (sintering temperature: 1360°C, heating rate: 10°C/min).

The variation of the relative density versus the sintering temperature for the micro-gears is presented in Fig. 17 where it can be seen that, the relative density of the specimens increases with the increment of the sintering temperature. It can be also observed that the sintering process makes the final density of the sintered bodies almost uniform. Homogeneous green relative densities equal 0.6, 0.62 and 0.64 have been used in simulation corresponding to the feedstocks loaded at 60%, 62% and 64%, respectively. It can be seen that the relative density of micro-gears increases with

increasing of the sintering temperature, the relative density is up 95% when the sintering temperature is 1360C. This indicated that the increase of the sintering temperature is in favour of the densification of stainless steel parts.

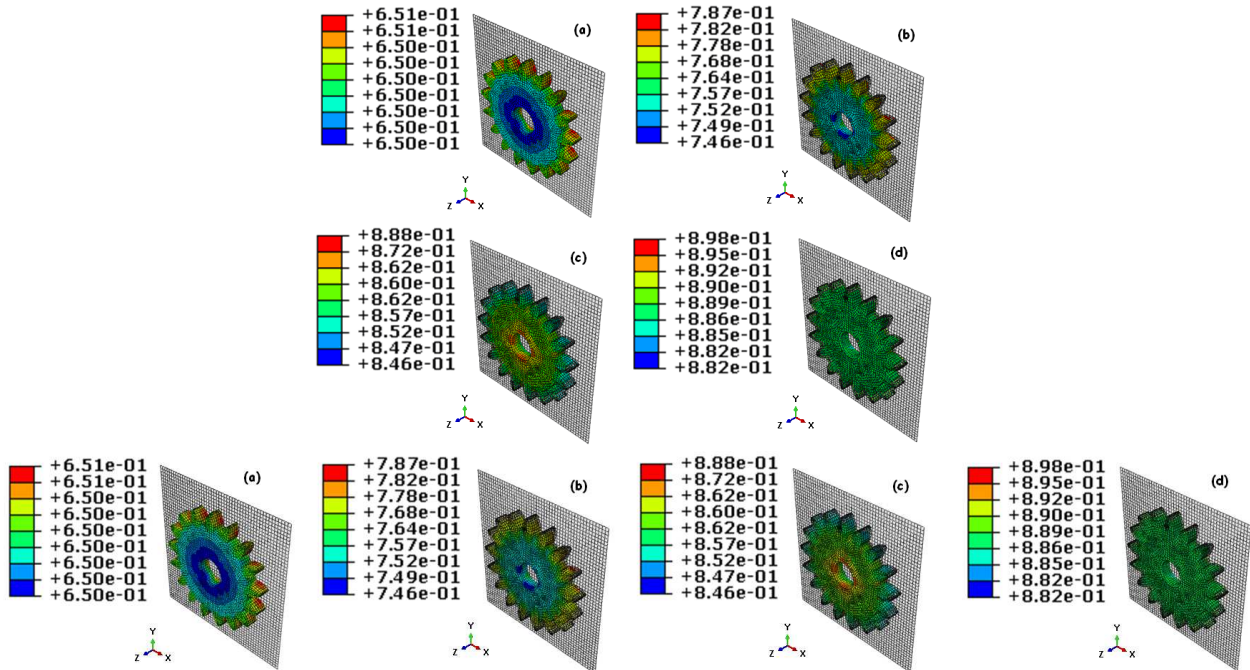


Fig. 17. Final distribution of the relative density in the micro-gears after sintering, obtained numerical simulation.: (a) 950°C, (b) 1150°C, (c) 1250°C and (d) 1360°C (solid loading: 60%, heating rate: 10°C/min).

5. Experimental validations

The dimensional analyses were carried out on the five sintered specimens injected with different feedstock loaded from 60% to 64%. The mean shrinkage in the main directions is illustrated in Figs. 18a and 18b. The results show that the feedstock loaded at 60%, with a sintering cycle utilizing a heating rate of 5°C/min results in the maximum shrinkage. Very high shrinkage in thickness direction was also observed for the micro-component injected with stainless steel feedstock loaded at 60%. This same phenomenon has been encountered by other researchers, such as N.H. Loh et al. [37]. The main parameters affecting the final part size have already been studied and include the metal powder morphology, binder ingredients and proportions, mixing conditions, mould design, moulding parameters, rheological behaviour of the moulding materials, debinding, sintering, equipment and even environmental conditions. Among these often

integrally related factors, the most sensitive are the powder volume loading and the mould design [37]. The numerically determined curves compare well with the experimental ones for the three different heating rates. Additionally, these results were confirmed by the choice of the sintering stress model and the identification method in our work.

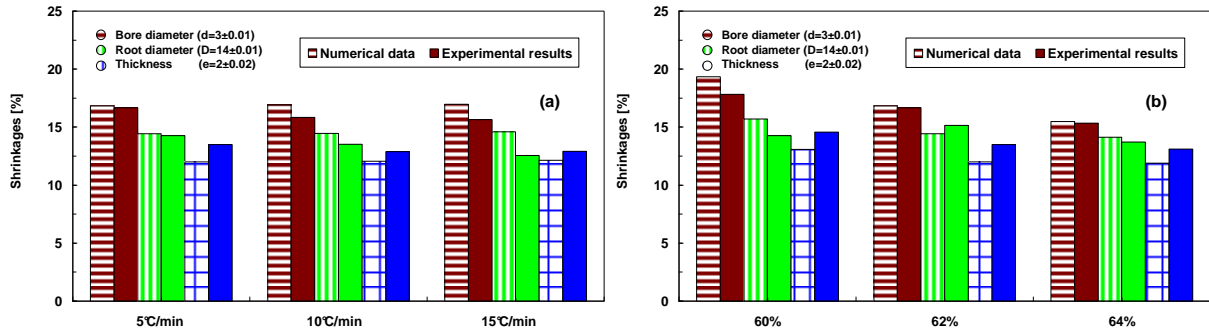


Fig. 18. Comparison between the experimental and numerical shrinkage for the micro-gear component sintered at 1360°C using (a) different heating rates (solid loadings: 62%) and (b) different solid loadings (heating rate: 5°C/min).

In addition, the relative densities of the sintered micro-gears were measured by the water displacement method (Archimede method) for the feedstocks loaded from 60% to 64%, as reported in Fig. 19. The relative density was calculated as the ratio of the measured density to the theoretical density. All specimens subjected to density measurements were ultrasonically cleaned in an alcohol bath for 10 min and rinsed in distilled water for an additional 10 min to remove any contaminants. The specimens were then dried with adsorbent paper towels. The average random and systematic errors in the density measurements were quantified as 2%. The sintered micro-gears using stainless steel feedstocks reached relative maximum densities between 92 to 97%.

As an example, the relative density distributions (for a solid loading of 60% and a heating rate of 5°C/min) of the sintered micro-gears are illustrated in Figs. 16 and 17. The relative densities were in perfect agreement with the experimental densities, especially for the sintering cycles with relatively low heating rates. The results from simulation are almost smaller than the ones from experiment; this is due to the fact that the identification tests in the vertical dilatometer have been carried out in an argon atmosphere instead of vacuum to prevent them from getting oxidised. As it is known, in some worse situations, the pores will be coarsen due to the inner expansion of the gas in the pores when the sintering is processed at high temperature [38], the consequence is that the slow down and

the reduction effect for densification, but there no gas trapped when the sintering stage is carried out in vacuum atmosphere, that's why the experimental results are always higher than the ones simulated by using the identified parameters from the vertical tests.

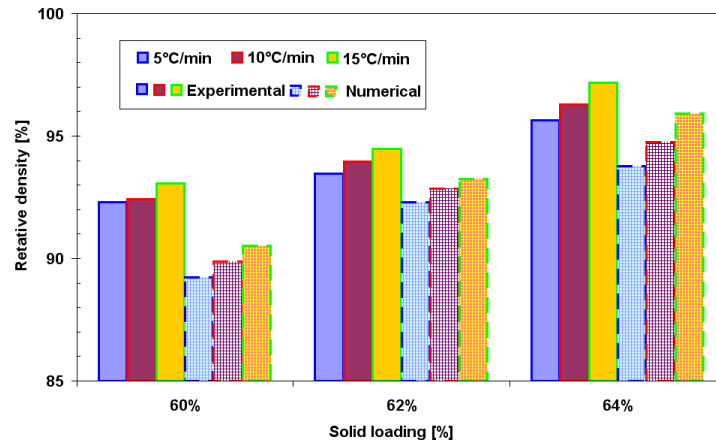


Fig. 19. Density variation of the sintered micro-gears fabricated using 316L stainless steel feedstock.

4. Conclusions

The paper summarizes experimental and numerical results carried out on micro-PIM process based on fine 316L stainless steel powders ($D_{50}=3.4\mu\text{m}$). The findings can be summarized as follows:

1. The micro-gears have been successfully injected corresponding to high powder volume loading (60%, 62%, 64% and 66%). Then injected micro-gears have thermally debinded and sintered by solid state diffusion according to different heating rates, which are adapted to get the micro-components free of defects with required mechanical and physical properties. Finally, geometrical and physical properties (shrinkage and relative density) of the resulting micro-gears have been measured.
2. The micro-gears exhibit very small shrinkage after injection and debinding. However, the components exhibit inhomogeneous shrinkage after sintering ranging from 14% to 18%, depending on the solid loading and sintering temperature and heating kinetics.
3. The main material and process parameters in the model have been identified accordingly to the sintering experiments through optimization based on the dilatometer experimental data. The FE model strongly depends upon the thermo-physical data and kinetics analysis of 316L

stainless steel parts. The model and resulting identified parameters have been implemented in a FE solver in order to simulate the sintering process.

4. The simulation of sintering step by using finite element simulation has been proven an efficient method to predict shrinkage of MIM components. The FE model result were compared to experimental results and showed satisfactory final shrinkage. We also demonstrate that the mechanical properties of these micro-gears can be predicted before sintering with high accuracy using FE methods.

In order to improve the accuracy of the simulation results, the powder inhomogeneity in the moulded parts has to be accounted as well as friction coefficient between the parts and sintering supports that should be properly defined.

References

- [1] J. Meng, N. H. Loh, G. Fu, B. Y. Tay, S. B. Tor, Micro powder injection moulding of alumina micro-channel part, *Journal of the European Ceramic Society*, 31 (2011) 1049-1056
- [2] D.F. Heaney, J.D. Gurosik, C. Binetj, Isotropic forming of porous structures via metal injection moulding, *J. Mater. Sci.*, 40 (2005) 973-981
- [3] G. Fu, N.H. Loh, S.B. Tor, Y. Murakoshi, R. Maeda, Replication of metal microstructures by micro powder injection moulding, *Mater. Des.*, 25 (2004) 729-733
- [4] F. Petzoldt Micro powder injection moulding – challenges and opportunities, *Powder Injection Moulding Int.*, 2 (2008) 37-42
- [5] R. Ruprecht, T. Gietzelt, K. Müller, V. Piötter, J. Haußelt, Injection molding of microstructured components from plastics, metals and ceramics, *Microsyst Technol*, 8 (2002) 351-358
- [6] B. Mamen, T. Barriere, J-C. Gelin, Investigations on thermal debinding process for fine 316L stainless steel feedstocks and identification of kinetic parameters from coupling experiments and finite element simulations, *Powder Technology*, 235 (2013) 192-202
- [7] R.M. German, The production of stainless steels by injection molding water atomized pre-alloy powders, *J. Injection Molding Technol.*, 1 (1997) 171-18
- [8] H. Riedel, A constitutive model for the finite-element simulation of sintering-distortions and stresses, *Ceram. Powder Sci. III* (1990) 619-630
- [9] R. Raj, Packing and Sintering of Two-Dimensional Structures Made from Bimodal Particle Size Distributions, *J. Am. Ceram. Soc.*, 70 (1987) 843-489
- [10] K. Mori, Finite element simulation of nonuniform shrinkage in sintering of ceramic powder compact, NUMIFORM92, Sophia-Antipolis, Rotterdam, (1992) 69-78
- [11] B.B. Hwang, S. Kobayashi, Deformation characterization of powdered metals in compaction, *Int. J. Mach. Tools Manuf.*, 30 (1990) 309-323
- [12] D.N. Lee, H.S. Kim, Plastic yield behaviour of porous metals, *Powder Metall.*, 35 (1992) 275-279

- [13] K. Biswas, Comparison of various plasticity models for metal powder compaction processes, *J. Mater. Process. Technol.*, 166 (2005) 107-115
- [14] N. Ramakrishnan, T.B. Bhat, V.S. Arunachalam, An analysis of pressure sintering by computer simulation, *Acta Metall.*, 32 (1984) 357-370
- [15] R.M. German, Computer modeling of sintering processes, *Int. J. Powder Metall. (USA)*, 38 (2002) 48-66
- [16] H. Lippmann, R. Iankov, Mathematical modeling of sintering during powder forming processes, *Int. J. Mech. Sci.*, 39 (1997) 585-596
- [17] E.A. Olevsky, Theory of sintering: from discrete to continuum, *Mater. Sci. Eng.*, 23 (1998) 41-100
- [18] A. Tsvetikh, W. Thompson, A. Easton, I. Freshwater, A geometrical finite element model of the sintering process of advanced ceramics, *Computational Materials Science* 3 (1995) 457-464
- [19] S.E. Schoenberg, D.J. Green, A.E. Segall, G.L. Messing, A.S. Grader, P.M. Halleck, Stresses and distortion due to green density gradients during densification. *J. Am. Ceram. Soc.*, 89 (2006) 3027-3033
- [20] J. Song, J.C. Gelin, T. Barrière, Experiments and numerical modelling of solid state sintering for 316L stainless steel components. *J. Mater. Proc. Tech.*, 177 (2006) 352-355
- [21] G.C. Kuczynski, Self diffusion in sintering of metallic particles, *Metal Transac.* 185 (1949) 169-178
- [22] R.L. Coble, Sintering of crystalline solids. I. Intermediate and final state diffusion models, *J. Appl. Phys.* 32 (1961) 787-792
- [23] J.K. McKenzie, R. Shuttleworth, A phenomenological theory of sintering, *Proceed. Phys. Society: B* 62 (1949) 833-852
- [24] T. Barriere, J.C. Gelin, B. Liu, Improving mould design and injection parameters in metal injection moulding by accurate 3D finite element simulation. *J. Mater. Process. Technol.* 125-126 (2002) 518-524
- [25] T. Barriere, B. Liu, J.C. Gelin, Determination of the optimal process parameters in metal injection molding from experiments and numerical modeling. *J. Mater. Process. Technol.* 143-144 (2003) 636-644
- [26] S. Nosewicz, J. Rojek, K. Pietrzak, M. Chmielewski, Viscoelastic discrete element model of powder sintering, *Powder Technology*, 246 (2013) 157-168
- [27] I. U. Mohsin, D. Lager, W. Hohenauer, C. Gierl, H. Danninger, Finite element sintering analysis of metal injection molded copper brown body using thermo-physical data and kinetics, *Computational Materials Science*, 53 (2012) 6-11
- [28] D. F. Heaney, R. Spina, Numerical analysis of debinding and sintering of MIM parts, *Journal of Materials Processing Technology*, 191 (2007) 385-389
- [29] M-S Jeong, J-H Yoo, S-H Rhim, S-K Lee, S-I Oh, A unified model for compaction and sintering behavior of powder processing, *Finite Elements in Analysis and Design*, 53 (2012) 56-62
- [30] M. Sahli, J.-C. Gelin, T. Barriere, Characterisation and replication of metallic micro-fluidic devices using three different powders processed by hot embossing, *Powder Technology* 246 (2013) 284-302
- [31] J. Song, T. Barriere, B. Liu, J.C. Gelin, G. Michel, Experimental and numerical analysis on sintering behaviours of injection moulded components in 316L stainless steel powders. *Powder Metall.*, 53 (2010) 295-304

- [32] R.K. Bordia, G.W. Scherer, On constrained sintering-I Constitutive model for a sintering body. *Acta Mater.*, 36 (1988) 2393-2397
- [33] A. Peterson, J. Agren, Constitutive behavior of WC-Co materials with different grain size sintered under load. *Acta Mater.*, 52 (2004) 1847-1858
- [34] R.M. German, Green body homogeneity effects on sintered tolerances, *Powder Metal.*, 47 (2004) 157-160
- [35] T. Kraft and H. Riedel, Numerical simulation of solid state sintering: model and application, *J. Eur. Ceram. Soc.*, 24 (2004) 345-361
- [36] M. Reiterer, T. Kraft, U. Janosovits and H. Riedel, Finite element simulation of cold isostatic pressing and sintering of SiC components, *Ceram. Int.*, 30 (2004) 177-183
- [37] N. H. Loh and R. M. German, Statistical analysis of shrinkage variation for powder injection molding, *J. Mater. Process. Technol.* 59 (1996) 278-284
- [38] R.M. German, *Powder Injection Molding*, Metal Powder Industries Federation, New Jersey (1990) 61-62.